Refractivity Estimation Using Multiple Elevation Angles

Peter Gerstoft, *Member, IEEE*, L. Ted Rogers, William S. Hodgkiss, *Member, IEEE*, and Lee J. Wagner

***Abstract*—Estimation of the atmospheric refractivity is important for the prediction of radar performance. Surface or elevated trapping layers formed by the outflow of relatively dry and warm air over a cooler body of water often result in the refractive structure-supporting–convergence-zone-like behavior and multimodal effects. The propagation under such conditions can be very sensitive to even small changes in the vertical and horizontal structure of refractivity. Obtaining *in situ* measurements of sufficient fidelity to estimate where intensifications in the electromagnetic field will occur is difficult.**

The authors previously have demonstrated the ability to infer refractivity parameters from grazing-incidence radar sea-clutter data. The radar system was the 2.8-GHz space range radar that overlooks the Atlantic Ocean in the vicinity of Wallops Island, VA. The forward modeling consisted of the mapping of an 11-parameter environmental model via an electromagnetic propagation model into the space of the radar clutter observations. A genetic algorithm was employed to optimize the objective function. Ground truth data were atmospheric soundings obtained by a helicopter flying a saw-tooth pattern. The overall result was that the ability to estimate the propagation within the duct itself was comparable to that of *in situ* measurements. However, the ability to characterize the region above the duct was quite poor.

Modern three—dimensional radars, however, have relatively narrow beams. Using these narrow beams at multiple elevations might resolve the ambiguity leading to the poor characterization in the region above the duct. Using radar data from the SPANDAR radar, it is demonstrated that such an approach is feasible and that more-robust estimates can be obtained by using two elevation angles and/or by constraining the solution to contain realistic refractivity profiles.

***Index Terms*—Radar clutter, refractivity estimation, SAGA.**

I. Introduction

AT THE frequencies of common radars (0.9–10 GHz), anomalous propagation effects at low altitudes are probably more the rule than the exception. Evaporation ducts, surface-based ducts (see Fig. 1) and subrefractive layers alter the return strength of both targets and clutter and, thus, alter radar performance. Radar performance assessments taking these ducting structures into account are presently based on *in situ* sampling, including bulk measurements of meteorological parameters from ship-mounted instruments for characterizing evaporation ducts and expendables (rocket sondes or radio sondes) for characterizing surface-based ducts [1].

This paper represents one in a series of steps in developing a capability to generate radar-performance predictions using the radar surface clutter, a through-the-sensor technique referred to as "refractivity from clutter" (RFC) [2]–[4]. Inferring an effective evaporation duct profile from radar clutter is a fairly simple one-parameter estimation problem [2]. Inferring parameters describing surface-based ducts from radar clutter is more difficult [3], [4]. Assuming that the radar cross section at the sea surface is not varying too much (what constitutes too much is an active area of research), the variation in clutter return is due to the two-way propagation from the radar to the reflection at the sea surface and, thus, it contains information about the atmospheric refractivity. It is an ill-posed inverse problem that has many parallels to full-field inversion methods employed in ocean acoustics. In fact, the research developed here is inspired by the advance in ocean acoustic matched field inversion over the last decade [5]–[7].

Compared to *in situ* sampling for estimating the effects of surface based ducts, RFC should reduce latency and provide azimuthal dependence. An important assumption is that the radar cross section is varying much less in range than the variation in two-way propagation loss. This was found to be the case for the data analyzed here [3]. This may not always be the case in a near-shore environment, where both wind and current can change strongly with range. Future research will address making the algorithm robust in the presence of range-varying sea-clutter radar cross section (RCS) and to quantify the degradation of inversion results as a function of the variability.

In previous work, the refractivity estimate was based on a single beam pointed at the horizon (0° elevation). To decrease the uncertainties in the estimates, the inversion here is implemented using two beams. The use of a higher beam adds information about the variation in returned power closer to the critical angle. The critical angle is the angle at which all energy is refracted back into the duct. Two beams are used for simplicity. While the use of three or more beams should lead to further improvements in the refractivity estimates, it will require further research to exploit the increased information.

In order to constrain the solution further, a soft constraint is put on the refractivity profile. This constraint also limits the strength of the duct. A hard constraint of this type was used in [3]. With a hard constraint, refractivity models exceeding a certain value are rejected. With a soft constraint, refractivity models are penalized (via the objective function) for unusual values; thus, these values are feasible provided that they have strong support in the data. The soft constraint and the use of single or

Manuscript received August 2, 2002; revised January 15, 2003. This work was supported by the Office of Naval Research Code 32.

P. Gerstoft and W. S. Hodgkiss are with Marine Physical Laboratory, University of California—San Diego, La Jolla, CA 92093-0238 USA (e-mail: gerstoft@ mpl.ucsd.edu).

L. T. Rogers and L. J. Wagner are with Atmospheric Propagation Branch, SPAWAR Systems Center, San Diego, CA 92152 USA.

Digital Object Identifier 10.1109/JOE.2003.816680

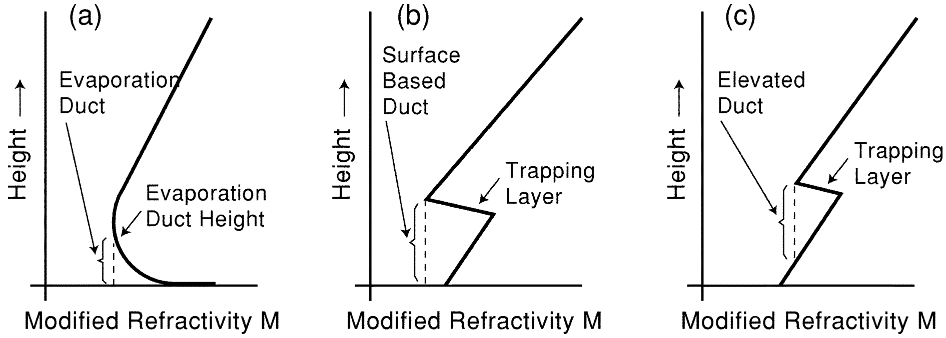

Fig. 1. Modified refractivity M versus height. (a) Evaporation duct (typical height 0–30 m). (b) Surface-based duct (typical height 30–500 m). (c) Elevated duct. The modified refractivity is the refractivity multiplied with 10^6 and transformed to correct for the curvature of the earth [8].

dual beams are considered both together and separately so that their marginal impacts can be assessed.

Details of the algorithm and assumptions can be found in Gerstoft *et al.* [3]. The same data have been analyzed by Vasudevan *et al.* [4]. Here, the main emphasis is on using multiple beams combined with a meteorological constraint to obtain stable and less-biased estimates of the range-dependent refractivity.

A. Surface-Based Ducts

Surface-based ducts appear approximately 15% of the time worldwide, 25% of the time off the southern California coast, and 50% of the time in the Persian Gulf [9]. While surface-based ducts are less common than evaporation ducts, their effects frequently are more dramatic. They often manifest themselves in a radar's plan position indicator as clutter rings (see Fig. 2; the Space Range Radar (SPANDAR) is described in Section II) and they can result in significant height errors for three–dimensional (3-D) radars as the lowest elevation scans become trapped on the surface instead of refracting upward, as would be expected for a standard atmosphere.

Surface-based ducts usually are associated with advection or subsidence of air masses and involve processes beyond those occurring in the surface layer. A common phenomena in some coastal regions is the advection of relatively warm and dry air over a cool ocean, sea, or lake, which forms a thermal internal boundary layer (TIBL) beginning at the wind-ward shore [10], [11]. The term "internal" is used because, at least at the land–sea interface, the planetary boundary layer (PBL) that has formed over land is still present. Near the wind-ward shore, the refractivity structure associated with the TIBL often looks like an evaporation duct. Sufficiently far downwind, the TIBL has been transformed to having a surface layer, a mixed layer, and an interfacial layer normally associated with the marine atmospheric boundary layer. By that point in range, the features of the original PBL have dissipated and the PBL and marine atmospheric boundary layer are synonymous. Thus, even under steady-state conditions, a horizontal transient is present in the structure of the TIBL.

Typically, the ducts associated with a TIBL are deeper than evaporation ducts (20–200 m versus 0–40 m). In addition to clutter rings, multiple modes [12] are excited as well, leading to a complex interference structure. It is hard to generalize about the sensitivity as the response is state dependent. But the refractivity structure of TIBL is often realized such that

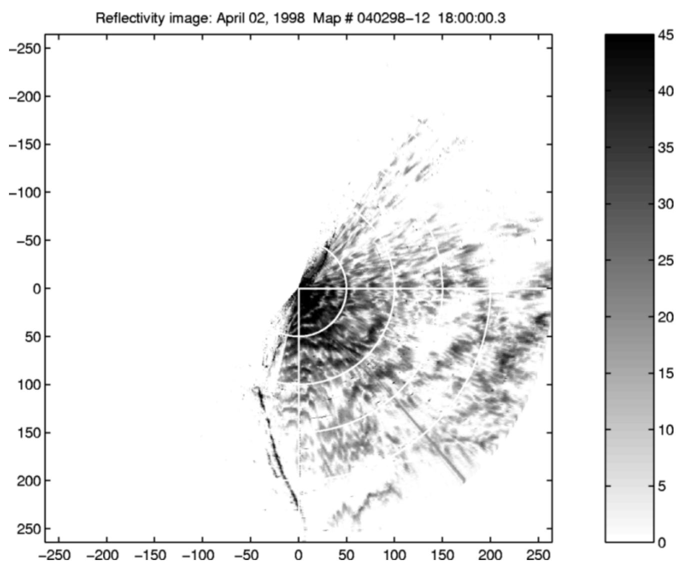

Fig. 2. Clutter map (signal-to-noise ratio, measured in dB) from SPANDAR corresponding to Wallops Run 12 (time 13:00 EST, see also Section II). The elevation angle is 0° and E/W and N/S ranges are in kilometers.

small changes in the structure result in very large changes in the electromagnetic (EM) field [13].

During scientific experiments, range-dependent soundings of the low-altitude refractivity structure obtained via helicopter have a level of fidelity such that the horizontal locations of intensification in the EM field are estimated with reasonable accuracy. But under real-world conditions where temporal and spatial sampling intervals are far less frequent, expecting more than a qualitative picture of where intensifications occur may be too optimistic. For example, the SEAWASP system [1] will normally utilize only range-independent refractivity at discrete temporal sampling intervals.

II. Data and Experiment

Radar and *in situ* validation data were obtained during the Wallops '98 measurement campaign [2]. The data presented here are from the surface-based ducting event that occurred on April 2, 1998 [3]. Radar data were obtained using the 2.8-GHz SPANDAR [14], which originally was designed as a tracking radar. It is equipped with (nominal) 4-MW and 1-MW transmitters and an 18.29-m parabolic antenna. The pulse width used corresponds to a 600-m range-bin width. With 446 range bins

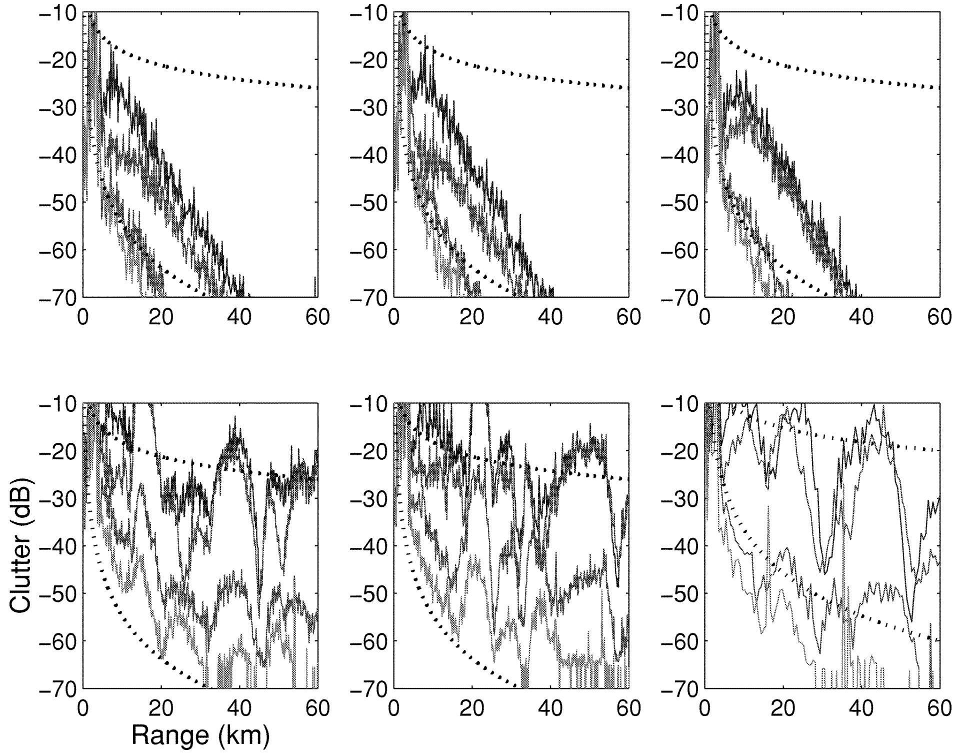

Fig. 3. The radar return for a nonducting (top row) and a ducting (bottom row) environment for 0, 0.1, 0.2, and 0.3° elevation angle for the SPANDAR radar. Note that the larger signals correspond to lower elevation angles and vice versa. The r^{-1} and r^{-3} decays are indicated as dotted lines. The nonducting returns were obtained on March 31, 1998 at 9:44, 11:24, and 12:13 EST, respectively. The ducting returns were obtained on April 2, 1998 at 14:26, 16:42, and 11:59 EST, respectively.

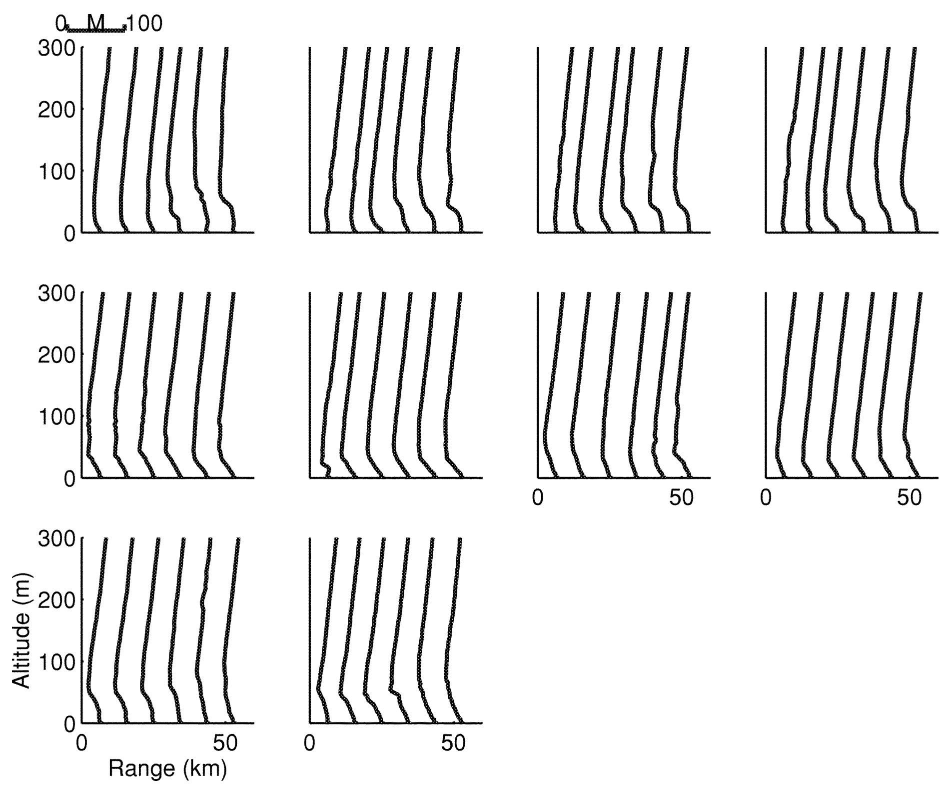

Fig. 4. Modified refractivity profiles (M-units) sequenced in time. The time for each profile is given in Table I. All refractivity profiles have been normalized to the same value (330 M-units) at sea level.

available, this provides maximum range of 267 km when the first range bin is set to 0 km. The beam pattern is approximated as a $\sin x/x$ beam with 0.4° beamwidth. The radar is equipped with a Sigmet Radar Data System that provides reflectivity, ve-

TABLE I
OBSERVATION TIMES (EST) FOR THE TEN HELICOPTER RUNS ON APRIL 2, 1998. THE HELICOPTER FLEW IN A SAW-TOOTH PATTERN OUT AND IN ALONG THE 150° RADIAL

Helicopter run	Time	Direction
1	8:47–09:05	out
2	09:07–09:32	in
3	09:33–09:57	out
4	09:58–10:26	in
5	12:26–12:50	out
6	12:52–13:17	in
7	13:19–13:49	out
8	13:51–14:14	in
9	15:59–16:27	out
10	16:29–16:52	in

TABLE II
OBSERVATION TIMES (EST) FOR THE 12 RADAR SCANS ON APRIL 2, 1998. THE HELICOPTER RUN CLOSEST IN TIME TO THE RADAR SCAN IS ALSO INDICATED

Scan	time	closest helicopter run
1	11:58:53	5
2	12:19:00	5
3	12:26:08	5
4	12:35:08	5
5	12:45:12	5
6	12:55:05	6
7	13:05:03	6
8	13:15:08	6
9	13:25:07	7
10	13:37:17	7
11	13:45:19	7
12	13:55:08	8

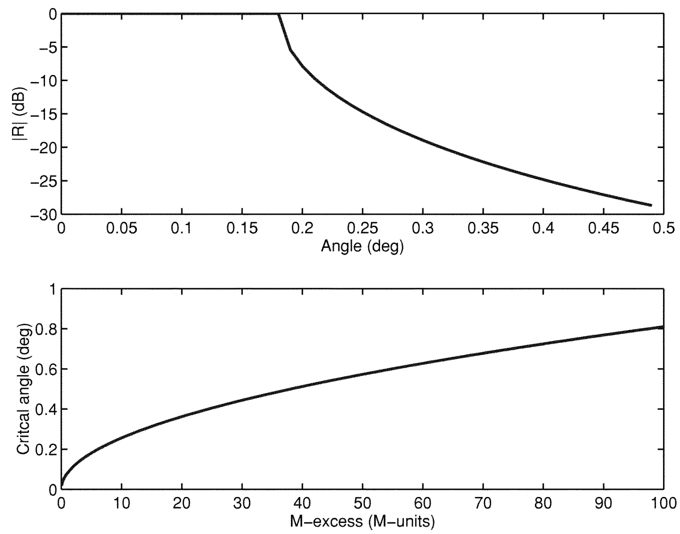

Fig. 5. (a) Reflection coefficient as a function of angle for an M-excess of $\Delta m = 5$ M-units. (b) Critical angle as a function of M-excess Δm. The M-value in layer one is 330 M-units.

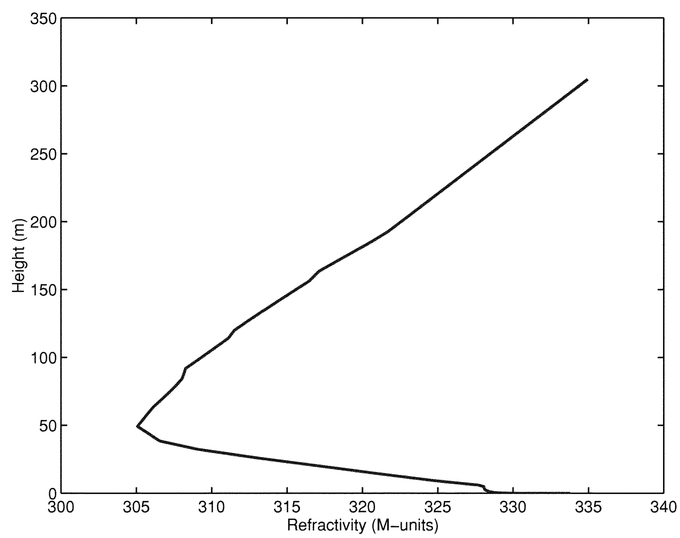

Fig. 6. M-profile used to generate the coverage diagrams in Fig. 5.

locity, time series, and spectra types of output [14]. However, for the Wallops'98 experiment, signal-to-noise ratio (SNR) was recorded rather than reflectivity.

A polar plot of SNR (or clutter map) at 0° elevation during a ducting event is shown in Fig. 2. The edges around radials 30° and 180°–200° are due to the coastline. The intensifications around ranges 130, 180, and 230 km are due to ducting propagation. To mitigate the effects of spurious targets (including sea spikes), the radar data used in the inversions are median filtered across range (1.8 km, three samples) and azimuth (5°, 13 samples).

An indication of the effect of a ducting layer can be seen in Fig. 3, where samples of radar returns are plotted for a day with no ducting (top row) and a day with ducting (bottom row). It is seen that the loss from the nonducting environment is decaying quickly with range. The r^{-3} decay corresponds to free-space propagation when corrected for the increased patch size with range. The behavior observed for the nonducting cases is described in detail in [2]. For the ducting environment, after about 20 km, the range falloff is essentially the same for all beam elevations, about r^{-1} corresponding to a ducting atmosphere corrected for increased patch size with range. For the higher elevation beams, the first 10 to 20 km show a stronger decay, whereas the shallower angles are trapped in the waveguide for shorter ranges and, thus, the falloff more quickly approaches the r^{-1} decay. Very characteristic of the ducting environment is the intensifications of the beam that occur at regular intervals. These are similar to the intensifications shown in Fig. 2 and contain useful information for carrying out the inversion.

In Fig. 4, observations of the refractive profiles are shown for times overlapping and exceeding the acquired radar data. The observation times for refractivity profiles and radar scans are given in Tables I and II, respectively. These profiles were measured by a helicopter flying out and in on the 150° radial from a point 4 km due east of the SPANDAR radar. During the

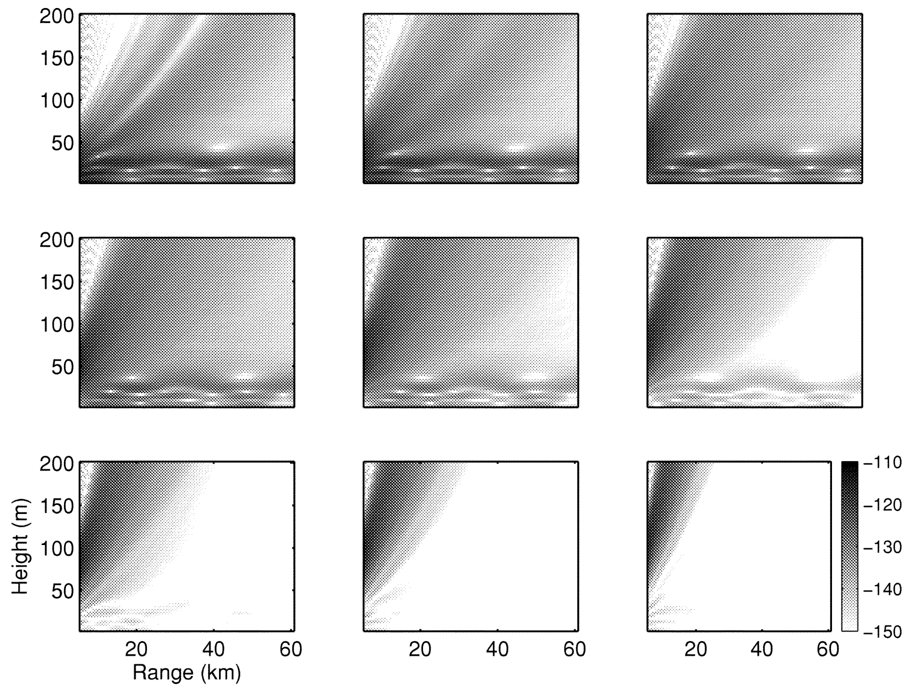

Fig. 7. Coverage diagrams (dB) for initial elevation angles (0–0.8° in steps of 0.1°).

flights, the helicopter would fly a saw-tooth up-and-down pattern and a single transect lasted about 30 min. The minimum in the M-profiles can be seen at around 50-m altitude. Note that there are strong range dependencies and that the refractive environment changes in a few hours. In the first frames, the duct height changes from 20 m near shore to 50 m further offshore. For the later profiles, the duct is more stable. Thus, it is quite demanding to observe these using radio sondes.

III. Objective Function

A composite objective function Φ is used to estimate the refractivity parameters $\mathbf{m}$ where both the match-to-the-radar data $\phi_{D,i}$ (i is the beam index) and the deviation from an *a priori* model ψ_M are used. For the data, two beams are used, one close to the ground (beam 1, 0° elevation) and one at a higher elevation (beam 2, 0.3° elevation)

$$\Phi(\mathbf{m}) = \phi_{D,1}(\mathbf{m}) + \lambda_D \phi_{D,2}(\mathbf{m}) + \lambda_M \psi_M(\mathbf{m}). \quad (1)$$

Based on experimentation with the data, the values of the Lagrangian multipliers were chosen as $\lambda_D = 0.25$ and $\lambda_M = 0.005$. The precise values are not that important. By having $\lambda_D < 1$, more emphasis is on the low-elevation data. λ_M was chosen so that the value of the first two terms of the objective function, $\phi_{D,1}(\mathbf{m}) + \lambda_D \phi_{D,2}(\mathbf{m})$, had slightly more sensitivity than the second part, $\lambda_M \psi_M(\mathbf{m})$.

An advantage of the objective function is that data from the first low-elevation beam (0°), which usually has more energy, is emphasized. The second beam is sufficiently elevated to provide information on the critical angle and, thus, the M-deficit (see Section III-B). The last term is a regularizing operator. Only if there is strong evidence in the data of a ducting environment will significant deviations from a standard M-profile be used. The objective function is minimized using a genetic algorithm [15], [16].

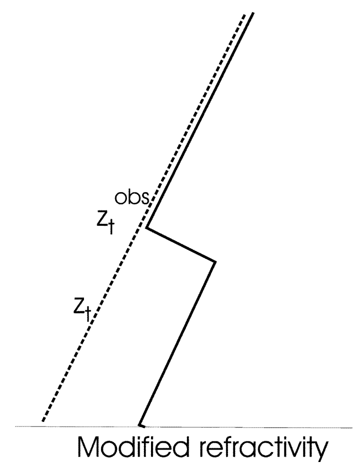

Fig. 8. Given a refractivity profile (solid line) with the top of the trapping layer z_t^{obs} and assuming adiabatic lapse rate, then all possible values of the top of the trapping layer z_t will lie on a line given by the adiabatic lapse rate (dashed line).

A. Data-Objective Function for Each Beam

For each beam i, a simple least-squares error measure is used. It is assumed that the difference (decibels) between the observed $\mathbf{P}_i^{\mathrm{obs}}$ and replica $\mathbf{P}_i(\mathbf{m})$ clutter is Gaussian ($\mathbf{P}_i$ and $\mathbf{P}_i^{\mathrm{obs}}$ are vectors of clutter return in range). The replica $\mathbf{P}_i(\mathbf{m})$ is based on the refractivity model in theAppendix, which is then fed though a tropospheric parabolic equation code (TPEM) [17]. This Gaussian assumption leads to a simple least-squares objective function

$$\phi_{D,i}(\mathbf{m}) = \mathbf{e}_i^T \mathbf{e}_i \quad (2)$$

where

$$\mathbf{e}_i = \mathbf{P}_i^{\mathrm{obs}} - \mathbf{P}_i(\mathbf{m}) - \widehat{T} \quad (3)$$

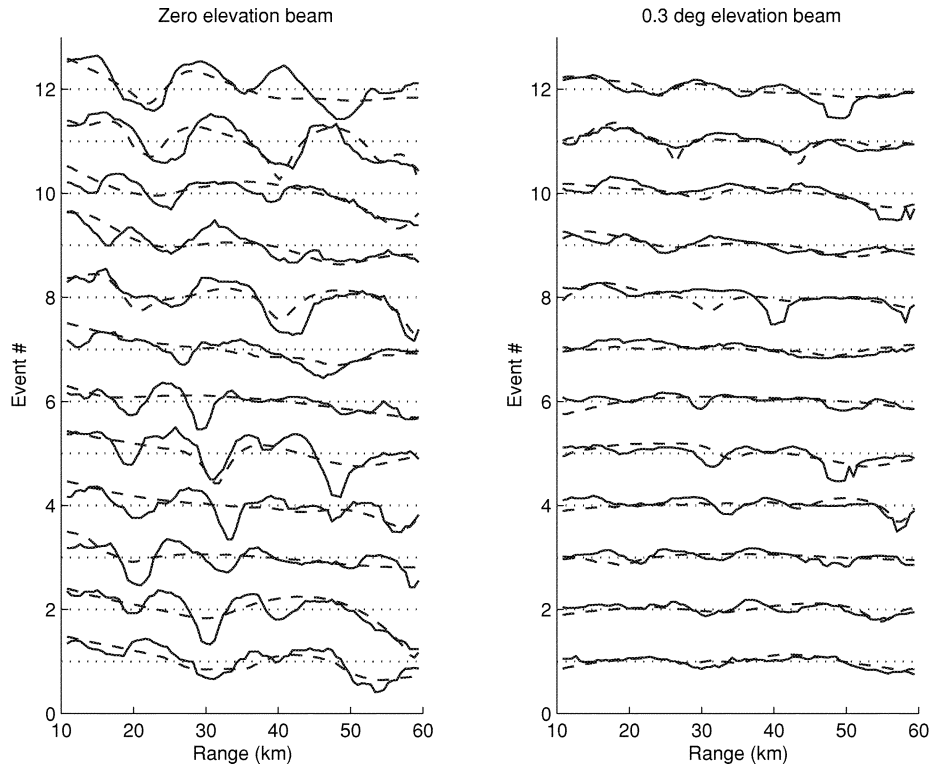

Fig. 9. Twelve realizations of observed (solid lines) and inverted (dashed lines) clutter return for an elevation angle of 0° (left) and 0.3° (right). The dotted line indicates the mean clutter return for each beam. There are 35 dB between each event for the 0° beam and 140 dB for the 0.3° beam.

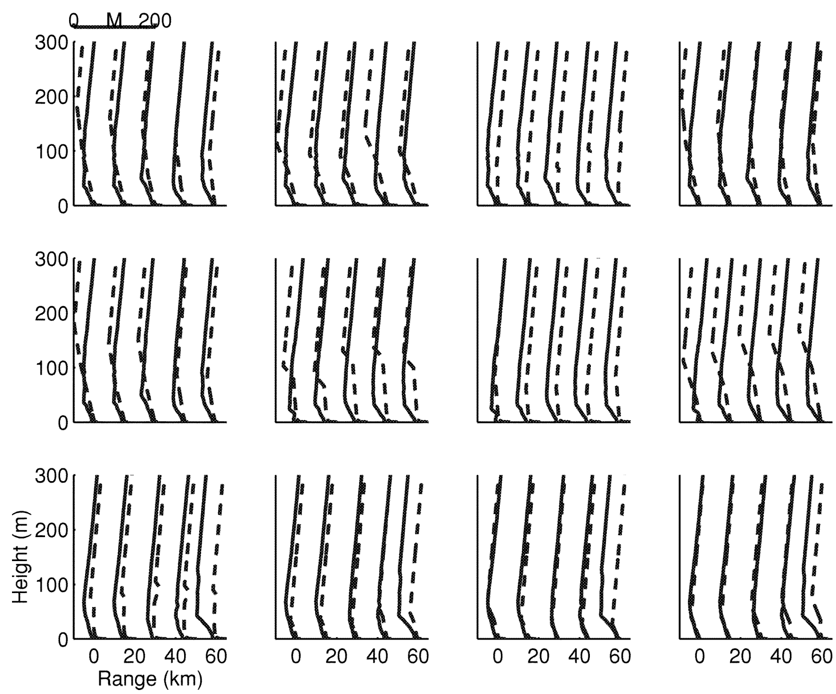

Fig. 10. The inverted refractivity profile (dashed line) compared to the measured profiles (solid line) using *one* beam at 0°.

$$\hat{T} = \frac{1}{N_{\text{beam}}} \sum_{i=1}^{N_{\text{beam}}} \overline{\mathbf{P}}_i^{\text{obs}} - \overline{\mathbf{P}}_i(\mathbf{m}) \tag{4}$$

and the bar denotes the mean across the elements in the vector (i.e., the mean over the ranges considered). $\widehat{T}$ is an estimated normalization constant that for each realization of $\mathbf{m}$, adjusted so that the objective function only depends on the variation in clutter return, but not on the absolute level of the clutter return. Note that the same normalization constant is used for each beam. Thus, the objective function is sensitive to the relative power between each beam.

B. Upper Beam

The upper beam is included to provide additional information about the critical angle. It does so by utilizing the relative

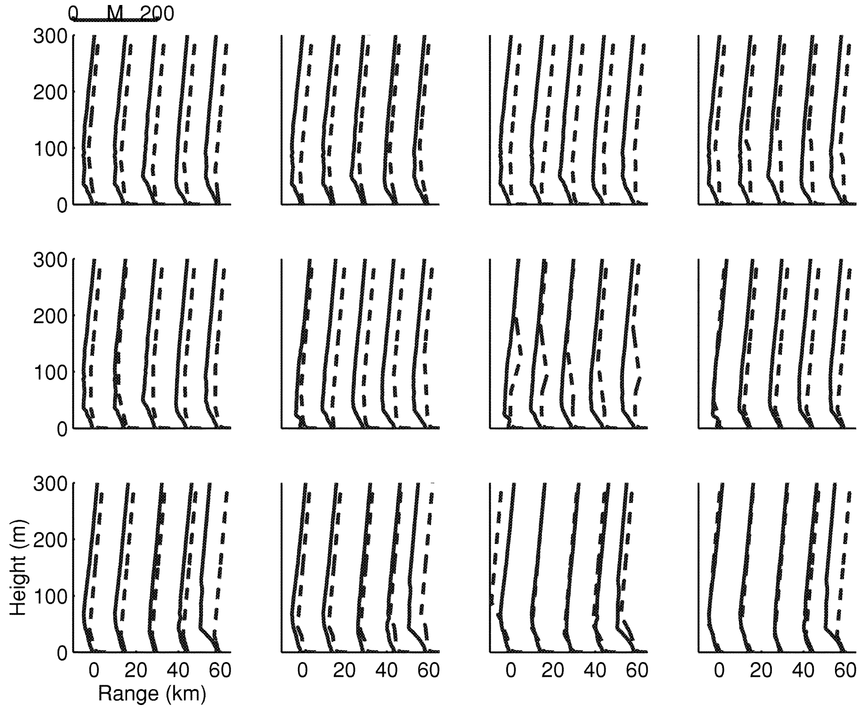

Fig. 11. The inverted refractivity profile (dashed line) compared to the measured profiles (solid line) using two beams.

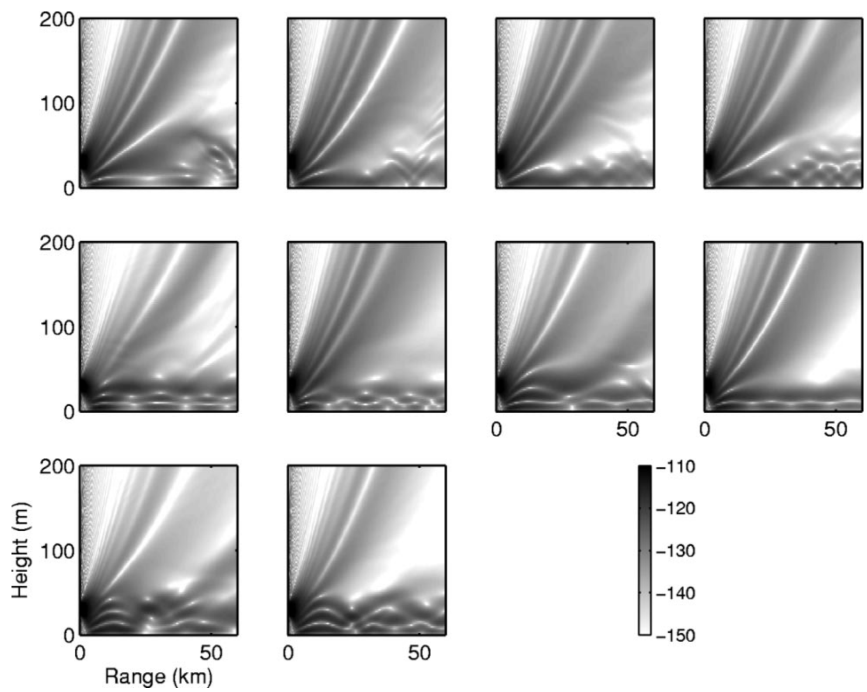

Fig. 12. Coverage diagram (dB) for each of the refractivity profiles in Fig. 5.

power between the two beams. In addition, it improves the refractivity estimates by having multiple observations of the same conditions.

For a plane wave propagating at an angle θ_1 in layer 1 with an M-value m_1 toward a layer 2 with an M-value m_2, the propagation angle θ_2 and reflection coefficient are given by

$$\theta_2 = \cos^{-1}\left[\cos(\theta_1)\frac{m_2}{m_1}\right] \tag{5}$$

$$R = \frac{\frac{m_2}{\sin(\theta_2)} - \frac{m_1}{\sin(\theta_1)}}{\frac{m_2}{\sin(\theta_2)} + \frac{m_1}{\sin(\theta_1)}}. \tag{6}$$

The critical angle, defined as the maximum angle that can be trapped, is

$$\begin{aligned}\alpha &= \mathrm{acos}\frac{1+10^{-6}m_2}{1+10^{-6}m_1}\\ &\approx .001\sqrt{2\Delta m}\end{aligned} \tag{7}$$

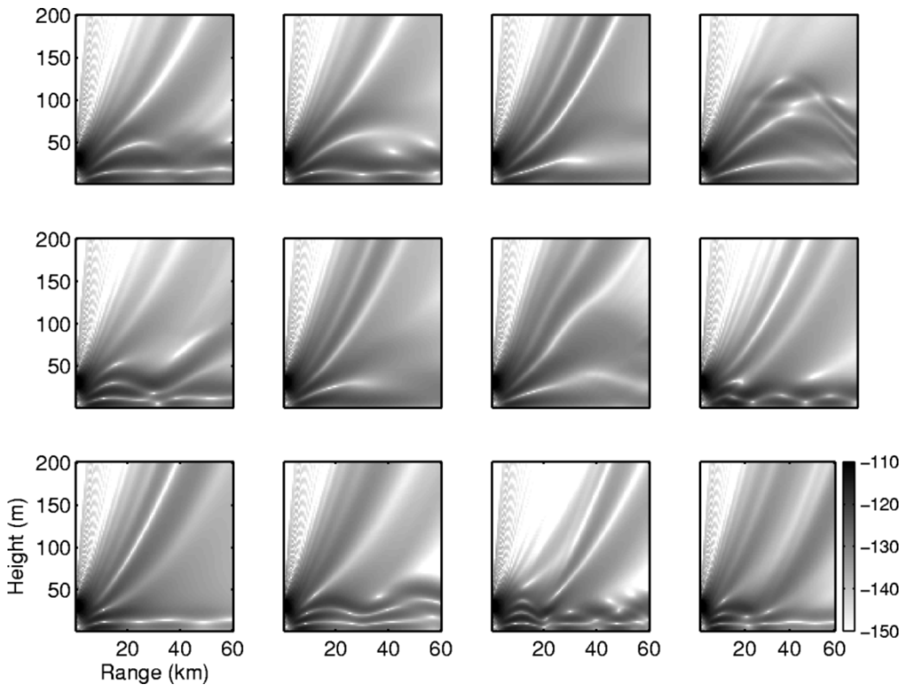

Fig. 13. The coverage diagrams (dB) from each of the 12 inverted refractivity profiles.

where $\Delta m = m_2 - m_1$. An example of the reflection coefficient is shown in Fig. 5(a) for $\Delta m = 5$ M-units. It is seen that, for this M-excess, the critical angle is 0.18°. The critical angle as determined by the above equation is shown in Fig. 5(b).

TPEM is used to generate propagation-loss coverage diagrams (shown in Fig. 7) using the profile given in Fig. 6 with the source at 35-m height. This gives a M-excess of 5 M-units and, thus, the plane-wave reflection coefficient as shown in Fig. 5 is representative. The radiation pattern was a $\sin x/x$ with a 0.4° beamwidth. The transition from having substantial energy trapped in the duct to having little if any energy trapped occurs over the range of 0.3°–0.5° in Fig. 5. This is larger than predicted from the plane-wave model (0.2°) because above the plane-wave critical-angle part of the beam will have energy radiating into the duct. Were a stronger duct modeled, that transition would occur at larger angles.

C. Climatological Information

The last term in (1) penalizes unrealistic profiles. For example, that could be done by penalizing the deviation from a standard profile. However, we use a constraint that is related to the strength of the duct, which is discussed below. Such a constraint could be formulated from climatological data [9], the output of numerical weather prediction models, or from local observations.

For an arbitrary refractivity profile, we will denote the top of the trapping layer as z_t^{obs} and the associated value of modified refractivity as $M(z_t^{\text{obs}})$. Based on simple physics (e.g., as described in Gossard [10]), it is possible to estimate a set of values for the top of the trapping layer z_t and its associated modified refractivity, as indicated in Fig. 8. For a surface duct, this will correspond to the minimum value of the M-profile. Assuming that the value of modified refractivity immediately above the sea surface remains constant, that the air mass above the top of the trapping layer remains constant in time, and that the lapse rate for refractivity in that air mass is c_{lap} leads to the relationship

$$M(z_t) \approx M\left(z_t^{\text{obs}}\right) + \left(z_t - z_t^{\text{obs}}\right) * c_{\text{lap}}. \tag{8}$$

c_{lap} is either taken as the slope for a convective boundary layer $(c_1 = 0.13 \text{ M-units/m})$ or average slope above the trapping layer $(c_2 = 0.118 \text{ M-units/m})$.

Use of (8) leads to the inequality constraint

$$dM_{\text{obs}} = M(0) + c_{\text{lap}} z_t - M(z_t) < dM_c \tag{9}$$

where dM_c is defined as the difference between the M-unit at the top of the duct and at the surface. Examination of the soundings shown in Fig. 4 gives $dM_c^{\text{obs}} = 60$ M-units. For other areas and soundings different values of dM_c will be observed. The value dM_c likely could also be derived from climatology. However, it is preferable to be able to do the inversion as a stand-alone procedure without depending on external information. Therefore, (9) is implemented as a soft constraint

$$\psi_M(\mathbf{m}) = \begin{cases} 0, & \text{for } dM_{\text{obs}} < dM_c \\ \frac{dM_{\text{obs}} - dM_c}{dM_c}, & \text{for } dM_{\text{obs}} > dM_c \end{cases} \tag{10}$$

where dM_c is chosen to 40 M-units. Thus, the constraint will not have any effect on profiles where the M-excess is less than 40 M-units. Implemented this way, large values of dM_{obs} are possible, provided that there is strong information about them in the data.

IV. Results

The SPANDAR data (Section II) is used to assess the impact of using two beam elevations and the soft meteorological constraint, both separately and together. The observed clutter data $\mathbf{P}_c^{\text{obs}}$ is taken from the 150° radial and 10–60-km range using clutter maps similar to Fig. 2. The horizon elevation beam used in the previous work [3] is augmented with data from the 0.3° elevation

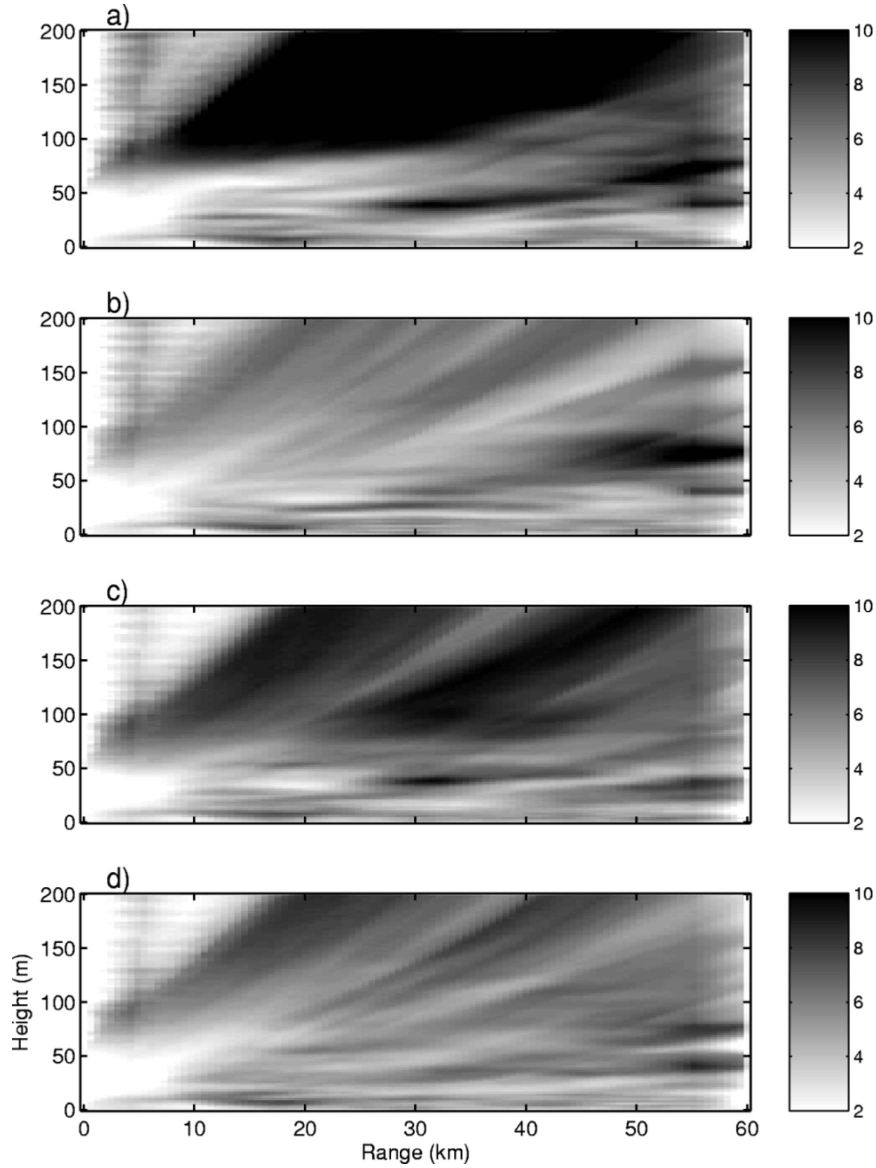

Fig. 14. Average propagation error (dB) for the 12 inversions. (a) One beam, (b) two beams, (c) one beam plus the meteorological constraint, and (d) two beams plus the meteorological constraint.

beam. As seen in Fig. 3, 0.3° is highest elevation at which the clutter data are generally above the noise floor of the receiver; different conditions might warrant using a higher or lower elevation. The data (solid) corresponding to 12 scans are shown in Fig. 9. Each of the 12 scans are inverted independently using the constrained multiple-angle approach and the optimal replica field is shown using a dashed line. The plot is designed to indicate the weighting of each beam in the inversion. Thus, the 0.3° has a $1/\lambda_D = 4$ times less sensitivity (there are 35 dB between each event for the 0° beam and 140 dB for the 0.3° beam).

The refractivity profile was modeled using the refractivity model in the Appendix and the radar return was then modeled using a parabolic equation code [17]. It is clear that the helicopter profiles in Fig. 4 show considerable horizontal variation. They lead to horizontal shifting of intensifications in the clutter, which may be realized in ways that might not be feasible for a horizontally homogeneous refractivity structure. One way of handling this "compliance" problem is to add degrees of freedom to the environmental model that describe horizontal variations in the refractivity structure. We add compliance to the model by incorporating parameters that are coefficients corresponding to the principal components of modeling the behavior of the base height as a Markov process with respect to range. For additional details, see [3].

The estimated refractivity profiles (dashed lines) are compared to the measured profiles (solid lines) for radar data at a single elevation and two elevations in Figs. 10 and 11, respectively. By visual inspection, it is clear that the duct strength is overestimated for runs 1, 2, 5, 6, and 8 when only a single elevation is used (Fig. 10). When two elevations are used, the duct strengths for those runs are much closer (Fig. 11). Based on the discussion in Section III-B, these are (a) expected results and (b) lead to better characterization of the "blind zone" above the duct.

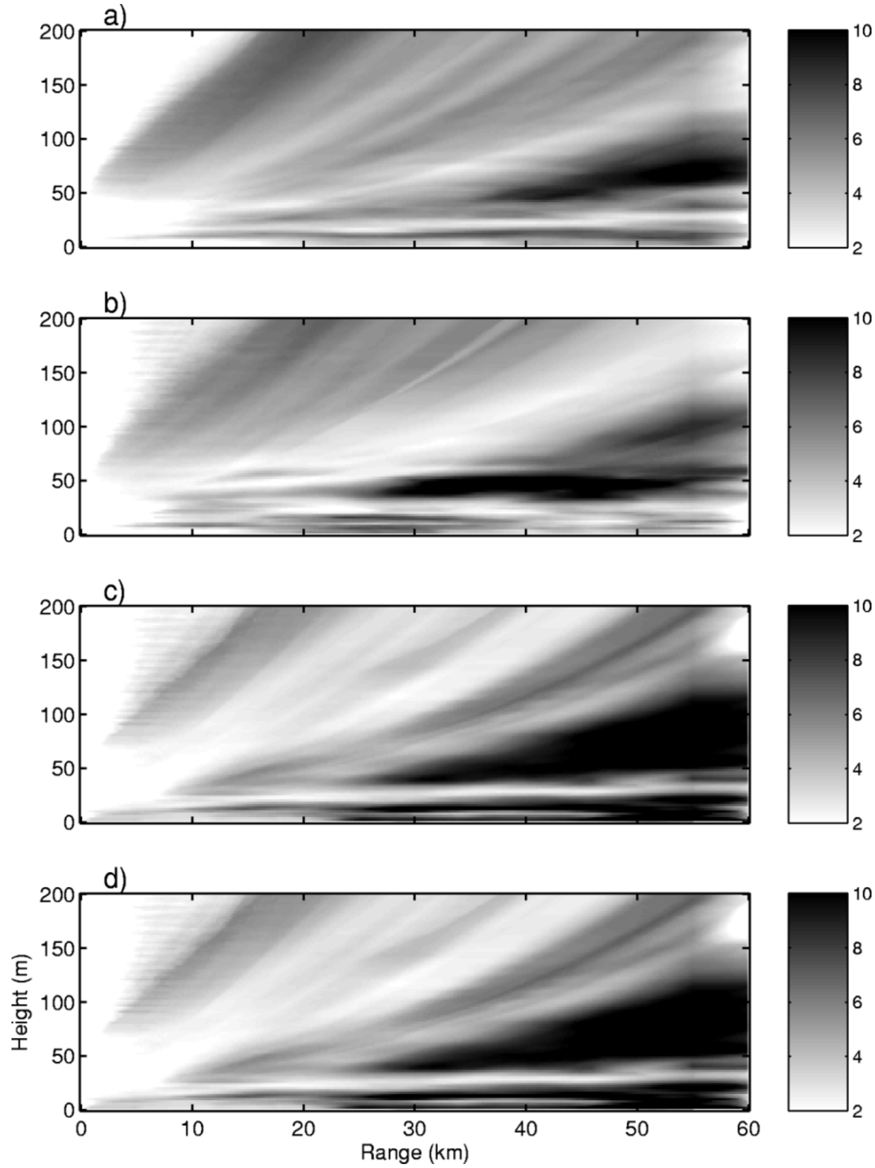

Fig. 15. Average propagation error (dB) between a coverage diagram for a full range-dependent run using the refractivity profiles as given in Fig. 5 and a range-independent run using just the profile at 20 km [(a) and (c)] or 50 km [(b) and (d)]. In (a) and (b), the helicopter profiles corresponding to the ones with radar observations (middle row in Fig. 5) are used. In (c) and (d), there is 4-h delay between the coverage diagram for the range-independent and range-dependent run (using the top row in Fig. 5).

Underestimating the degree of ducting should be as much of a matter of concern as overestimation. It is clearly evident that duct strengths are underestimated in some instances—cases 3 and 7 when using a single elevation and cases 3 and 6 when using dual elevations.

Propagation loss is calculated from observed and radar-inferred refractivity profiles (Fig. 4), generated using two beams. The coverage diagrams for the observed soundings and the inverted profiles are shown in Figs. 12 and 13, respectively. Note that the times of the 12 radar observations overlap the last six range-dependent soundings and that no radar data are available for the first four soundings. Summary results for using radar data to estimate the propagation calculations based on the range-dependent soundings are shown in Fig. 14. The following approaches were tested: 1) a single beam, 2) two beams, 3) a single beam plus the meteorological constraint, and 4) two beams plus the meteorological constraint. From the plots, it is clearly seen that using just a single beam in the inversion cannot estimate the propagation loss above the trapping layer [Fig. 14(b)]. Incorporating either the meteorological constraint and/or using two beams reduces this error significantly.

A. Discussion

The helicopter profiles are not easy to obtain in practice. In fact, having a single radiosonde or rocket sonde might be considered a best case scenario. As noted by Goldhirsh and Dockery [13], this leads to systematic errors in the coverage diagrams. Additionally, the interval between soundings may be from 10 min. to several hours. Two benchmarks are developed based on these factors. Having a single sounding is simulated by assuming the vertical refractivity profile at all ranges equal to the helicopter refractivity profile at either 20 or 50 km. One benchmark is the accuracy of these "range-independent" environments in estimating the propagation loss predicted using the range-dependent soundings. The effects of time lags can be considered as well, since the helicopter soundings were started several hours before the radar observations. The second benchmark is thus based on using soundings 4 h prior to the range-dependent soundings.

The benchmark results are given in Fig. 15. In general, the on-time 20- and 50-km benchmarks have roughly the same error, while the time-delayed versions of the same show substantially more error. In particular, the region within the duct (0–50 m) at ranges of 20 km and greater shows errors that exceed 10 dB over at least half the region.

In comparison with benchmarks, the following is observed for the configurations considered:

1) For propagation within the duct, the goodness of the radar-inferred propagation predictions is somewhat less than that of the on-time benchmarks. However, those differences are on the order of a few decibels. In comparison with the time-delayed benchmarks, the radar-inferred propagation loss is substantially better. The reason for this is the substantially different propagation conditions in the morning than in the afternoon (see Fig. 4).
2) For propagation above the duct, it appears that only the use of dual beams without the soft constraint approaches the goodness of the on-time benchmarks. It is arguable that the use of dual beams with the soft constraint approach the goodness of the time-delayed benchmarks. Clearly, the unconstrained single-beam inversion shows no skill in this regard, while the skill of the constrained beam is limited.

V. Conclusion

An inversion algorithm has been implemented to invert for refractivity profiles from radar sea-clutter data using the horizon elevation beam by itself and in conjunction with the same clutter observed at a second elevation, so as to exploit the influence of the critical angle of propagation. Both beam combinations are implemented with and without a soft constraint as might be based on climatology, the output of a numerical weather prediction model, or *in situ* observation.

Radar-inferred propagation calculation are compared to propagation calculated from range-dependent *in situ* refractivity profiles obtained by helicopter. Performance benchmarks are based on range-independent sampling having either no time delay or a 4-h time delay. These benchmarks arise from considering how *in situ* sampling would be implemented in a practical scenario.

For all four possible combinations of the number of beams and whether or not the soft constraint is used, the goodness of the propagation estimates based on the radar-inferred environments appear closer to that of the on-time benchmarks than the time-delayed benchmarks. Only the radar-inferred propagation estimates based on two beams appear to estimate the propagation above the duct roughly as well as do the benchmarks.

Clearly, one day of observations are not sufficient to make a broad conclusion, particularly about the relative goodness of soundings versus radar-inferred values of refractivity. However, we are confident on the following.

1) The clutter inversion problem is ill-posed and using additional information as, e.g., a meteorological constrain or radar data at multiple elevations, will improve the refractivity estimation.
2) Using radar data at multiple elevations where one or more of the elevations is near the critical angle may significantly improve inversion results.
3) Consideration of typical time-lag values associated with a particular form of sensing is necessary in determining their relative merits.

Appendix
Modeling of Refractive Environment

Surface-based ducts can be associated with either convective or stable boundary layers, e.g., [18]. A typical case for the convective boundary layer is that the surface layer within the boundary layer is unstable (e.g., $T_{\rm sea} > T_{\rm air}$) and the vertical structure is described by Monin–Obukhov similarity theory. Above the surface layer is the mixed layer, where the potential temperature and specific humidity are largely height independent. The gradient of modified refractivity dM/dz within the mixed layer will tend to a value of 0.13 M-units/meter [10]. The capping inversion is the region between the mixed layer and the free troposphere and can have strongly negative modified refractivity gradients. Often the change in the gradient is quite pronounced, producing a "sharp top" [19].

With the stable boundary layer, the surface layer is stable (e.g., $T_{\rm sea} < T_{\rm air}$) and the gradient of modified refractivity will transition from negative to positive values within distances ranging from a few to many tens of meters. There is no mixed layer or capping inversion per se, but as the profiles from the Wallops '98 experiment indicate (Fig. 4), the profiles of modified refractivity can be quite complex.

The environmental model illustrated in Fig. 16 usually can describe refractivity profiles corresponding to either convective or stable cases. The model consists of an evaporation duct profile (for the surface layer) and line segments corresponding to the mixed layer, capping inversion, and free troposphere for the case of a convective boundary layer. By letting the slope in the segment corresponding to the mixed layer take on negative values (as opposed to having a slope fixed at 0.13 M-units/m), the model can also describe profiles associated with stable layers. However, when a stable layer is present, the mixed and inversion layers do not conform to the meteorological definition. The value of modified refractivity as a function of height is given by

$$M(z) = M_0 + \begin{cases} M_1 + c_0\left(z - \delta \log \frac{z}{z_0}\right), & \text{for } z < z_d \\ c_1 z, & \text{for } z_d > z < z_b \\ c_1 z_b - M_d \frac{z - z_b}{z_{\rm thick}}, & \text{for } z_b < z < z_t \\ c_1 z_b - M_d + c_2(z - z_t), & \text{for } z_t < z \end{cases} \tag{A1}$$

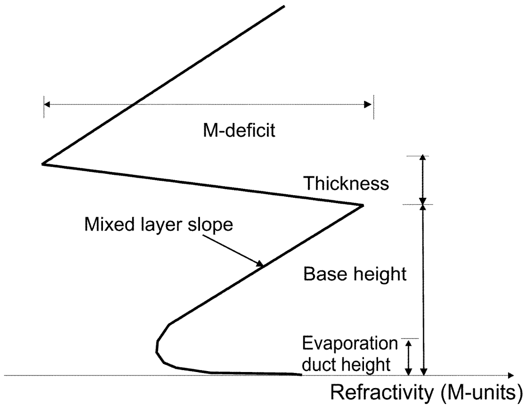

Fig. 16. Five-parameter refractivity model.

where

- the expression $c_0\big(z - \delta \log(z/z_0)\big)$ with roughness factor $z_0 = 0.000\,15$ and $c_0 = 0.13$ corresponds to the neutral refractivity profile [20]. δ is the evaporation duct height;
- c_1 is the slope in the mixed layer. A feasible range is $[-1, 0.4]\ \mathrm{M\text{-}units/m}$. This includes the typical value of 0.13 M-units/m for a convective boundary layer [10];
- c_2 is the slope above the trapping layer. Typical values are 0.13 M-units/m corresponding to an adiabatic equilibrium or 0.118 M-units/m, which is consistent with the mean over the whole of the U.S. Because the profiles are upward refracting, this is not a sensitive parameter and 0.118 M-units/m was used here;
- z_d is determined by

$$z_d = \begin{cases} \frac{\delta}{1-\frac{c_1}{c_0}}, & \text{for } 0 < \frac{1}{1-\frac{c_1}{c_0}} > 2 \\ 2\delta, & \text{otherwise} \end{cases} \qquad \text{(A2)}$$

  subject to $z_d < z_b$. When $z_d = 2\delta$, the lower condition in (A2), the slope is not continuous.
- z_b is the trapping-layer base height. We choose to allow it to vary from 0 to 500 m. When the base height is 0 m, a bilinear profile is obtained.
- z_{thick} is thickness of the inversion layer. A typical range is $[0, 100]\ \mathrm{m}$.
- z_t is determined by

$$z_t = z_b + z_{\mathrm{thick}}. \qquad \text{(A3)}$$

- $M_0 = 330\ \mathrm{M\text{-}units}$ is the offset of the M-profile, determined as the value at which the mixed layer slope intersects $z = 0$. For the field calculated at a single frequency, the offset is not important and is chosen arbitrarily.
- M_1 is determined by

$$M_1 = c_0 \delta \log \frac{z_d}{z_0} + z_d(c_1 - c_0). \qquad \text{(A4)}$$

- M_d is M-deficit of the inversion layer. We allow it to vary from $[0, 100]\ \mathrm{M\text{-}units}$.

Acknowledgment

The assistance of K. Anderson, SPAWAR, is appreciated. The helicopter-refractivity profiles were kindly supplied by D. Dockery, John Hopkins University, Baltimore, MD.

References

[1] J. J. Sylvester, G. C. Konstanzer, J. R. Rottier, G. D. Dockery, and J. R. Rowland, "Aegis anti-air warfare tactical decision aids," *Johns Hopkins APL Tech. Dig.*, vol. 22, no. 4, pp. 473–487, Oct.–Dec. 2001.

[2] L. T. Rogers, C. P. Hattan, and J. K. Stapleton, "Estimating evaporation duct heights from radar sea clutter," *Radio Science*, vol. 35, no. 4, pp. 955–966, Jul.–Aug. 2000.

[3] P. Gerstoft, L. T. Rogers, J. Krolik, and W. S. Hodgkiss, "Inversion for refractivity parameters from radar sea clutter," Radio Science, vol. 38, no. 3, 2002, to be published.

[4] S. Vasuvedan, R. H. Anderson, J. L. Krolik, L. T. Rodgers, and P. Gerstoft, "Recursive bayesian electromagnetic refractivity estimation from radar sea clutter," *IEEE Trans. Signal Process.*, submitted for publication.

[5] A. B. Baggeroer, W. A. Kuperman, and P. N. Mikhalevsky, "An overview of matched field methods in ocean acoustics," *IEEE J. Oceanic Eng.*, vol. 18, pp. 401–424, Oct. 1993.

[6] A. Tolstoy, *Matched Field Processing for Underwater Acoustics*. Singapore: World Scientific, 1993.

[7] O. Diachok, A. Caiti, P. Gerstoft, and H. Schmidt, Eds., *Full Field Inversion Methods in Ocean and Seismo-Acoustics*. Dordrecth, The Netherlands: Kluwer, 1995.

[8] M. P. M. Hall, *Effects of the Troposphere on Radio Communications*. Stevenage, Herts, U.K.: Peter Peregrinus, 1979.

[9] W. Patterson. (1992) Ducting Climatology Summary. SPAWAR Systems Center, San Diego, CA. [Online]. Available: http://sunspot.spawar.navy.mil/2858/index.html

[10] E. E. Gossard and R. G. Strauch, *Radar Observations of Clear Air and Clouds*. Dordrecth, The Netherlands: Elsevier, 1983.

[11] I. M. Brooks, A. K. Goroch, and D. P. Rogers, "Observations of strong surface radar ducts over the persian gulf," *J. Applied Meteorology*, vol. 38, pp. 1293–1310, Sept. 1999.

[12] K. G. Budden, *The Waveguide Mode Theory of Wave Propagation*. Englewood Cliffs, NJ: Prentice-Hall, 1961.

[13] J. Goldhirsh and D. Dockery, "Propagation factor errors due to the assumption of lateral homogeneity," *Radio Science*, vol. 33, no. 2, pp. 239–249, Mar.–Apr. 1998.

[14] R. W. Stahl and D. A. Crippen, *An Experimenters Guide to the NASA Atmospheric Sciences Research Facility*. Wallops, VA: Goddard Space Flight Center, Wallops Flight Facility, 1994.

[15] P. Gerstoft, "Inversion of seismoacoustic data using genetic algorithms and a posteriori probability distributions," *J. Acoust. Soc. Amer.*, vol. 95, no. 2, pp. 770–782, Feb. 1994.

[16] ——, (1997) SAGA Users Guide 2.0, An Inversion Software Package. SACLANT Undersea Research Centre. [Online]. Available: http://www.mpl.ucsd.edu/people/gerstoft/saga

[17] A. E. Barrios, "A terrain parabolic equation model for propagation in the troposphere," *IEEE Trans. Antennas Propagat.*, vol. 42, pp. 90–98, Jan. 1994.

[18] R. B. Stull, *An Introduction to Boundary Layer Meteorology*. Dordrecth, The Netherlands: Kluwer, 1998.

[19] J. C. Wyngaard, N. L. Seaman, S. J. Kimmel, M. Otte, X. Di, and K. E. Gilbert, "Concepts, observations, and simulation of refractive index turbulence in the lower atmosphere," *Radio Science*, vol. 36, no. 4, pp. 643–643, Jul.–Aug. 2001.

[20] R. A. Paulus, "Evaporation duct effects on sea clutter," *Radio Science*, vol. 38, no. 11, pp. 1765–1771, Nov. 1990.

Peter Gerstoft (M'03) received the M.Sc. and Ph.D. degrees from the Technical University of Denmark, Lyngby, in 1983 and 1986, respectively, and the M.Sc. degree from the University of Western Ontario, London, ON, Canada, in 1984.

From 1987 to 1992, he was with Ødegaard and Danneskiold-Samsøe, Copenhagen, Denmark, working on forward modeling and inversion for seismic exploration, with a year as Visiting Scientist at the Massachusetts Institute of Technology, Cambridge. From 1992 to 1997, he was Senior Scientist at SACLANT Undersea Research Centre, La Spezia, Italy, where he developed the SAGA inversion code, which is used for ocean acoustic and electromagnetic signals. Since 1997, he has been with the Marine Physical Laboratory, University of California, San Diego. His research interests include global optimization; modeling; and inversion of acoustic, elastic, and electromagnetic signals.

L. Ted Rogers was born in Miami, FL, on Feb. 14, 1954. He received the B.S. degree in engineering sciences from the University of Florida, Gainesville, in 1983 and the M.S. degree in applied mathematics from San Diego State University, San Diego, CA, in 1990.

From 1983 to 1988, he served as a Surface Warfare Officer in the U.S. Navy. Since 1990, he has been with what is currently called the Space and Naval Warfare Systems Center, San Diego, CA. His primary research interest is in improving estimation of the refractivity structure associated with the marine atmospheric boundary layer through combining *in situ* and remotely sensed observation with data from numerical weather-prediction models.

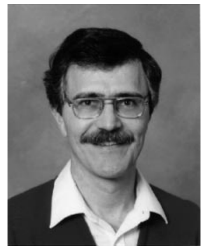

William S. Hodgkiss (S'68–M'75) was born in Bellefonte, PA, on August 20, 1950. He received the B.S.E.E. degree from Bucknell University, Lewisburg, PA, in 1972 and the MS and Ph.D. degrees in electrical engineering from Duke University, Durham, NC, in 1973 and 1975, respectively.

From 1975 to 1977, he was with the Naval Ocean Systems Center, San Diego, CA. From 1977 to 1978, he was a Faculty Member in the Electrical Engineering Department, Bucknell University, Lewisburg, PA. Since 1978, he has been a Member of the Faculty, Scripps Institution of Oceanography, University of California, San Diego, and on the staff of the Marine Physical Laboratory, where he is currently Deputy Director. His present research interests are in the areas of adaptive array processing, propagation modeling, and environmental inversions with applications of these to underwater acoustics and electromagnetic wave propagation.

Dr. Hodgkiss is a Fellow of the Acoustical Society of America.

Lee J. Wagner received the B.S. and M.S. degrees in electrical engineering from San Diego State University, San Diego, CA, in 1993 and 1998, respectively.

In 1999, he joined the Atmospheric Propagation Branch at the Space and Naval Warfare Systems Center, San Diego, CA. He is involved primarily in the estimation of the refractivity structure combining *in situ* and remotely sensed observations.